Beam-pointing fluctuations in a gain-guided Raman amplifier

S. J. Kuo, D. T. Smithey, and M. G. Raymer

Department of Physics and Chemical Physics Institute, University of Oregon, Eugene, Oregon 97403

We present a measurement of the beam-pointing fluctuations of a transient Raman-amplifier output using an interferometric method and a theoretical treatment of the three-dimensional, spatial propagation of transient stimulated Raman scattering (SRS) including the fluctuations of the Stokes field giving rise to the beam-pointing fluctuations. The theory is based on an effective steady-state model for the transient SRS process. By using nonorthogonal transverse modes to expand the field, we incorporate the effects of excess spontaneous-emission noise associated with gain-guided amplifiers. The agreement of the measurements with the theoretical treatment demonstrates that the beam-pointing jitter is caused by quantum noise. The beam-pointing fluctuations increase as the Fresnel number of the interaction volume increases because more spatial modes are excited.

PACS number(s): 42.50.−p, 42.65.Dr, 42.55.Vc, 42.60.Jf

I. INTRODUCTION

Macroscopic quantum-mechanical fluctuations of light have been observed in a number of single-pass stimulated optical processes, such as superfluorescence [1], amplified spontaneous emission [2], and stimulated Raman scattering SRS [3]. These processes involve light initiated from spontaneous noise and amplified to a macroscopic level in a gain medium without a cavity. In SRS the fluctuations have been observed in the pulse energy [3–5], and in the temporal [6], spectral [7], and spatial domains. The macroscopic fluctuation of the spatial distribution of the Stokes light in SRS was first observed by Henesian, Swift, and Murray [8] and later by Kuo, Radzewicz, and Raymer [9]. The fluctuation of the pointing angle of the Stokes output from a transient Raman amplifier is an example of the macroscopic fluctuations of SRS due to quantum-mechanical uncertainty of the initiation from spontaneous emission. For large Fresnel number of the interaction volume, the spatial fluctuation is manifest in the shape of the intensity distribution. For Fresnel number of the order unity, the fluctuation is primarily in the beam-pointing direction rather than the shape, which is approximately Gaussian. The beam-pointing fluctuation in SRS was predicted by Walmsley [10] and was observed by us recently [11]. In this paper, we present in detail the experimental studies and the theory for treating transient, three-dimensional (3D) propagation of SRS and the resulting beam-pointing fluctuations.

The Raman amplifier is an example of a gain-guided amplifier. Gain-guided amplifiers belong to a class of non-Hermitian optical systems, other examples of which include unstable resonators [12] and resonators with strong output couplings [13]. In these systems, the eigenmodes of the homogeneous, transverse part of the wave equation are nonorthogonal, and are called biorthogonal. This leads to the interpretation that is referred to as excess spontaneous emission. Ordinary spontaneous noise refers to the fact that there is one extra photon emitted per mode due to quantum-mechanical uncertainty for

systems governed by Hermitian wave equations. For non-Hermitian systems, there is more than one extra photon per mode emitted, and this is characterized by the excess-noise factor [14,15] which is always greater than unity. This interpretation has been used to understand the power spectrum of semiconductor lasers [16] which is observed to be broader than that predicted from standard laser theory which assumes orthogonal eigenmodes. Recently the nonorthogonal mode-expansion approach has been applied to single-pass x-ray lasers to predict their transverse spatial coherence properties [17]. The x-ray laser involves photons initiated from spontaneous emission and amplified in an open-ended gain-guided medium, in a fashion similar to that in a Raman amplifier [18]. Since nonuniform, high gain is usually employed in these processes, gain discrimination between different nonorthogonal modes is expected to be significant. The implications of the nonorthogonal modes have been studied in detail by several researchers [14,15,19,20], yet a consensus on the understanding of these excess-noise effects is lacking.

A study of the beam-pointing fluctuations of the Raman-amplifier output provides some additional insights into the excess-noise effect. To guarantee that the angular distribution of the output does not change during a single pulse due to collisional dephasing, a transient condition must be met, i.e., the pump pulse duration must be short compared to the inverse Raman linewidth of the medium. Then the beam-pointing angle is determined by the relative amplitudes of the eigenmodes. The amplitudes are correlated in the case of nonorthogonal modes, in contrast to the case of orthogonal modes. This correlation directly affects the beam propagation direction.

To treat the statistics of the beam-pointing angles of the Raman amplifier, the detailed spatial distribution of the Stokes field is needed. Three-dimensional propagation in the steady-state case has been treated previously [17,21]. An analytic, transient theory for 3D SRS that accounts for a nonuniform spatial profile of the pump

pulse will be presented here. This complements previous treatments of transient, 3D SRS that dealt with large Fresnel number cases and did not provide analytic solutions for the Stokes field [22]. The theory of SRS developed in this paper using biorthogonal eigenmodes is applied to calculate the statistics of the beam-pointing angle using a formalism first developed by Walmsley for orthogonal modes [10] and extended here for biorthogonal modes.

Walmsley defined the beam-pointing direction via the mean, transverse propagation vector for a single pulse: $\mathbf{K}_T = (\mathbf{K}_T)_x \hat{e}_x + (\mathbf{K}_T)_y \hat{e}_y$, where the x component is given by

$$(\mathbf{K}_T)_x \equiv \frac{-i \int d\tau \int dx \int dy \, E_S^*(\mathbf{r},\tau)(\partial/\partial x)E_S(\mathbf{r},\tau)}{\int d\tau \int dx \int dy \, |E_S(\mathbf{r},\tau)|^2} ,$$

(1a)

and similarly for the y component. In Fourier-transform space, this becomes

$$\mathbf{K}_T = \frac{\int d\tau \int d^2k \, \mathbf{k}|\tilde{E}_S(\mathbf{k},L,\tau)|^2}{\int d\tau \int d^2k \, |\tilde{E}_S(\mathbf{k},L,\tau)|^2}$$

(1b)

where $E_S(\mathbf{r},\tau)$ is the Stokes field at the output face ($z = L$) of a Raman cell, and $\tilde{E}_S(\mathbf{k},L,\tau)$ is its 2D, transverse Fourier transform. This definition relates to fluctuations of pointing directions in three dimensions. We have found it convenient to study the pointing fluctuation in the x-z plane. If one measures only along a "slice" at $y = 0$, then the mean transverse k value of that field is

$$K_x \equiv \frac{-i \int d\tau \int dx \, E_S^*(x,y =0,\tau)(\partial/\partial x)E_S(x,y =0,\tau)}{\int d\tau \int dx \, |E_S(x,y =0,\tau)|^2} .$$

(2)

We will refer to this as the "sliced-beam" k value, and to Walmsley's definition, $\mathbf{K}_T$, as the "whole-beam" k vector.

To measure the beam-pointing angle relative to the propagation axis defined by the pump laser, care must be taken to separate the pointing fluctuation of the pump laser relative to the laboratory frame. To achieve this, we have measured the relative beam-pointing angles of two Stokes beams generated from the same pump beam in different portions of the hydrogen gas cell. Two-beam interference can be used for this purpose because the periodicity of the interference pattern is determined from the difference of the transverse components of the Stokes-beam wave vectors. By splitting the laser pulse into equal halves to pump the Raman medium, two independent Stokes beams with nearly fixed relative orientation can be generated. The two beams are combined in an interferometric setup similar to a Mach-Zehnder interferometer to allow measurement of the single-shot interference patterns. The statistical fluctuations of the beam-pointing angles measured in this manner are studied for various Fresnel numbers of the interaction volume.

It is found that the Stokes-beam propagation angle

fluctuates on the order of the diffraction-limited angle for Fresnel number equal to five, and less for smaller Fresnel number. This results because the number of (biorthogonal) transverse modes having positive gain scales approximately linearly with Fresnel number F. This scaling is a result of gain guiding, and contrasts with the F^2 scaling familiar in the free-space case. Reasonably good agreement between the data and the theory based on biorthogonal modes is found.

II. EXPERIMENT

The apparatus used to generate two independent Stokes fields and single-shot interference patterns is shown in Fig. 1. The linearly polarized pump-laser pulse is split at BS1 into two equal-amplitude beams and sent into the 1-m-long Raman cell containing hydrogen gas at 40 atm. The two beams are 1 cm apart, nearly parallel to each other, and their intensity is equal to each other to within 0.2%. A metal divider is inserted between the two beams in the Raman cell to ensure two independent interaction volumes. The zero-point motion of the molecules in one interaction volume is not correlated to those in the other volume [23]. Therefore, for Stokes light initiated from quantum noise, the two Stokes fields are statistically independent, even though they are generated from the same pump pulse. The two output beams are combined on beam splitter BS2 at a nominal angle of 1–3 mrad to form interference patterns for both the Stokes light and the pump light. These patterns are viewed separately using the dichroic mirror DC and colored-glass filters FL1 and FL2. The lenses $L2$ and $L3$ image the light from near the output face of the cell onto the camera, so the fringes observed are originated from the near field of the Raman-amplifier output.

The spatial profile of the pump-laser beam is controlled by collimation using a pair of lenses indicated as $L1$. The Fresnel number of the interaction volume, which is defined to be the cross-sectional area of the pump beam divided by the Stokes wavelength and interaction length
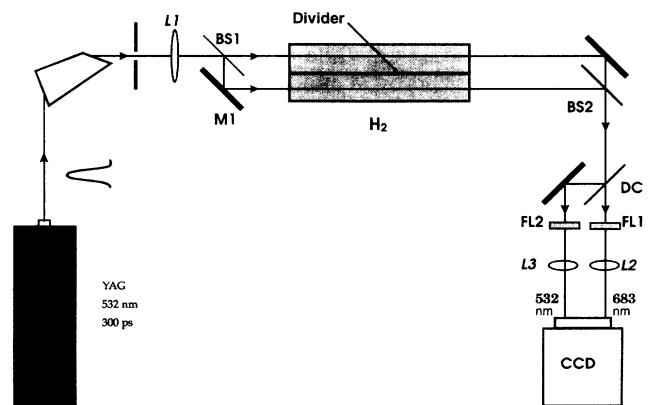

FIG. 1. Apparatus for generating two independent Stokes beams which are combined to produce an interference pattern, whose spatial frequency is indicative of the relative angle between the two beams. Interference patterns of Stokes light and pump light are recorded on a CCD camera.

$(F = \pi a_{1/2}^2 / \lambda_S L)$, is varied from 1.1 to 4.3. For each Fresnel number, the beam spot sizes are measured for several positions along the center axis of the Raman cell. For the smallest Fresnel number, corresponding to a beam waist (half-width at half-maximum intensity) $a_{1/2}$ equal to 0.49 mm near the center of the cell, the spot radius at 20 cm from the cell entrance is approximately 6% larger than the beam waist, while the spot corresponding to a waist of 0.97 mm, the beam radius at either end of the Raman cell is no more than 8% larger than that at the cell center.

The laser pulse is produced by a mode-locked, Q-switched, and cavity-dumped, neodymium-doped yttrium aluminum garnet (Nd:YAG) laser [24], and is amplified at 10 Hz and frequency doubled to yield a 532-nm pulse with duration (full width half maximum, FWHM) $\tau_L = 300$ ps and energy up to 6 mJ. The steady-state gain coefficient at 40 atm for the $Q(1)$ vibrational transition in H_2 is 2.5×10^{-9} cm/W [25]. The SRS is kept well below saturation (conversion efficiency $\leq 10^{-4}$) to allow a simple interpretation and modeling of the quantum origin of the beam-pointing fluctuations. The duration of the Stokes pulses is measured with a streak camera to be $\tau_S = 170$ ps as shown in Fig. 2. The collision linewidth of the $Q(1)$ transition at this pressure is $\Gamma = 6.5 \times 10^9$ rad/s [25]. Because $\Gamma \tau_S = 1.1$, the SRS is transient, in the high-gain but unsaturated case. This guarantees that the phase of the Stokes pulse, although random from shot to shot, does not drift during a given pulse, allowing observation of high-contrast interference fringes [26].

An example of the single-shot spatial interference patterns recorded by the charged-coupled-device (CCD) camera is shown in Fig. 3(a). The upper half is a picture of a Stokes interference pattern, the lower half is the interference pattern of the pump field. Each interference pattern is a single realization of the flux-density distribution $J(x,y)$, which is the intensity integrated over the duration of the pulse. Figure 3(b) shows the single-pixel-wide flux density $J(x)$ at some fixed y coordinate. To collect a sufficiently large number of data samples, we store only a two-pixel-wide flux-density distribution near the center of the pattern ($y = 0$) for each realization, along with the pump pulse energy. Figure 3(c) shows the two-pixel-wide flux density recorded for 128 successive realizations, arranged vertically one after another. Fluctuations in the depth of modulation and locations of the fringe maxima are easily observable for the Stokes data, while the pump fringes are quite stable, limited only by
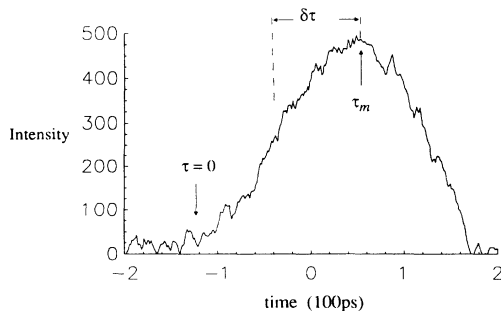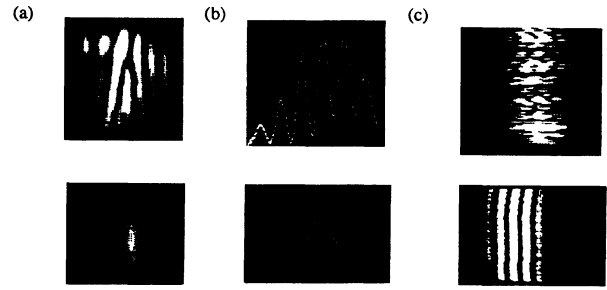

FIG. 3. Single-shot interference patterns of Stokes light and pump light recorded by the CCD camera: Stokes patterns in upper half, pump patterns in lower half (a) interference patterns from a single shot, (b) flux density $J(x)$ obtained from a single-pixel-wide trace of (a), (c) two-pixel-wide samples of interference patterns from 100 successive shots.

interferometer jitter. To minimize the effects caused by variations in the pump energy and by the mechanical instabilities, simultaneous measurements of the Stokes and pump interference patterns, along with the pump pulse energy for each shot, were undertaken. For each Fresnel number, several thousand realizations of the Stokes and the pump interference fringes were recorded over some range of the varying pump energy values. Using the pulse-energy information of the pump, data ensembles were constructed from samples that correspond to nearly constant Stokes gain, typically by restricting the energy of the pump pulses to be within $\pm 1\%$ of some average.

Two examples of the single-shot flux density exhibiting fluctuations in the fringe spacing are shown in Fig. 4 to illustrate fluctuation in the fringe spacing, resulting from the beam-pointing jitter. To obtain the relative beam-pointing angle of the two beams from each realization of the flux density $J(x)$, a fast Fourier transform is applied to $J(x)$. The Fourier spectrum $\tilde{J}(k_x)$ has three components, a dc peak, a component on the negative angular-frequency side $\tilde{J}_-(k_x)$, and a component on the positive angular-frequency side $\tilde{J}_+(k_x)$. The absolute square of the positive component is averaged over a sufficiently large angular-frequency range (k_1, k_2) to obtain a mean spatial frequency for the fringe on a single shot:

$$\bar{k}_x = \frac{\int_{k_1}^{k_2} dk \, k \, |\tilde{J}_+(k)|^2}{\int_{k_1}^{k_2} dk \, |\tilde{J}_+(k)|^2} . \qquad (3)$$
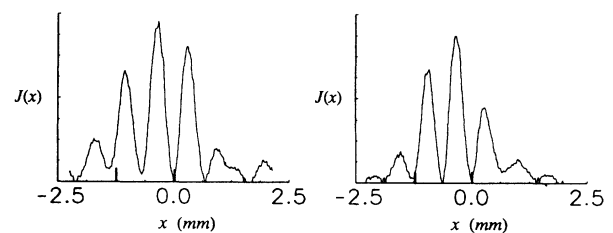

FIG. 2. Temporal profile of a Stokes pulse.

FIG. 4. Two examples of single-shot interference fringes of Stokes light. Different periodicities are observable, indicating fluctuations of the relative beam-pointing angle.
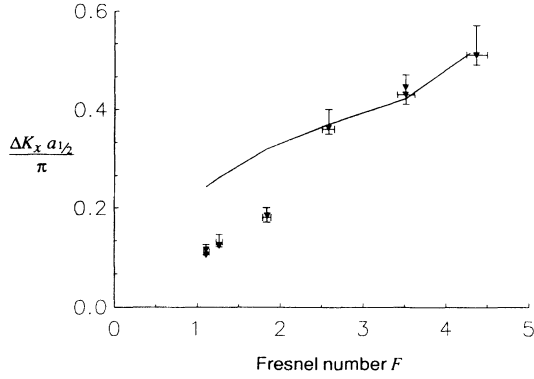
FIG. 5. Triangles show measured standard deviation of the mean transverse k value. The error bars are lower-bound estimates of variations due to digitization, pump fluctuations, and statistical errors. The solid curve shows predictions from the biorthogonal-mode model that incorporates excess-noise effects, from Eq. (43).

This quantity contains information about the beam-pointing fluctuation in the x direction only, and we argue that it is essentially equivalent to $\bar{k}_x = K_{x1} - K_{x2}$, where K_{x1} and K_{x2} are given by Eq. (2) for each beam separately. This is clearly so for plane waves, and will be discussed in more detail in Sec. IV.

Because the two beams are statistically independent, we can obtain the standard deviation ΔK_x of the transverse k value of a single beam via $\Delta K_x = \Delta \bar{k}_x / \sqrt{2}$, where $\Delta \bar{k}_x$ is the standard deviation of $\bar{k}_x$ from the two-beam measurements. The quantity $\Delta K_x a_{1/2} / \pi$ is plotted versus Fresnel number in Fig. 5. The plotted quantity is equal to the standard deviation of single-beam-pointing angle divided by the diffraction-limited angle defined by the pump-beam aperture with radius equal to $a_{1/2}$. Each data point, shown as a triangle, corresponds to a data set with between 300 and 700 measurements and steady-state gain coefficient $g_0 L$ having a precise value ($\pm 1\%$) somewhere in the range from 33 to 37. The theoretical predictions of the fluctuations of the sliced-beam pointing angle are shown as a solid line. Before proceeding to discuss the significance of the experimental results, we present the theoretical treatment of transient 3D Stokes generation and the statistics of the beam-pointing angles.

III. QUANTUM THEORY OF TRANSIENT, 3D STIMULATED LIGHT SCATTERING

A. Equations of motion

Consider transient Stokes generation in a Raman medium pumped by a pulsed laser field of finite duration and transverse dimension. The operator Maxwell-Bloch equations for Stokes generation in the paraxial approximation are [27,28]

$$\left[\nabla_T^2 + 2ik_S \frac{\partial}{\partial z} \right] \hat{E}_S(\mathbf{r},\tau) = -2k_S \kappa_2^* E_L^*(\mathbf{r},\tau) \hat{Q}(\mathbf{r},\tau) , \quad (4a)$$

$$\frac{\partial}{\partial \tau} \hat{Q}(\mathbf{r},\tau) = -i\kappa_1^* E_L(\mathbf{r},\tau) \hat{E}_S(\mathbf{r},\tau) , \quad (4b)$$

where the Stokes field operator is $\hat{E}_S(\mathbf{r},t) \exp(ik_S z - i\omega_S t) + \text{H.a.}$, the nonresonant medium polarization field at the Stokes frequency is proportional to $E_L^*(\mathbf{r},t) \hat{Q}(\mathbf{r},t) \exp(ik_S z - i\omega_S t) + \text{H.a.}$, the classical pump-laser field is $E_L^*(\mathbf{r},t) \exp(ik_L z - i\omega_L t) + \text{c.c.}$, and $\hat{Q}(\mathbf{r},t)$ is the slowly varying envelope of the medium excitation (in our case molecular vibration) oscillating at frequency $\omega_{21} = \omega_L - \omega_S$ and propagating with wave number $k_L - k_S$. ∇_T^2 is the transverse Laplacian. The equations are written in terms of the local, or retarded, time $\tau = t - z/c$. Group-velocity dispersion is neglected. Dephasing of the medium excitation is also neglected when the transient condition is met [27]. The coupling constants can be expressed in terms of the molecular polarizability derivative $\partial \alpha / \partial q$ as $\kappa_1^* = [\pi/(m\hbar\omega_{21})]^{1/2}(\partial \alpha / \partial q)$ and $\kappa_2^* = N\hbar\omega_S \kappa_1 / c$, where m is the reduced mass of the vibrational mode. The boundary conditions are that the Stokes field is localized around the z axis, and that it is equal to the vacuum, or free, field at $z = 0$. The polarization operator is initially δ correlated in space,

$$\langle \hat{Q}^\dagger(\mathbf{r}_1, 0) \hat{Q}(\mathbf{r}_2, 0) \rangle = \frac{1}{N} \delta^3(\mathbf{r}_1 - \mathbf{r}_2) , \quad (5)$$

where N is the molecular density, and $\tau = 0$ represents an instant in local time just before the arrival of the laser pulse at the points $\mathbf{r}_1, \mathbf{r}_2$ in the interaction region. The brackets indicate a quantum ensemble average.

Because there is little depletion or group-velocity dispersion, the laser envelope is assumed to be factorizable into a space-dependent part and a time-dependent part,

$$E_L(\mathbf{r},\tau) = E_L(\mathbf{r}) E_0(\tau) , \quad (6)$$

where $E_L(\mathbf{r})$ is the spatial envelope of the Stokes field and $E_0(\tau)$ is the peak-normalized temporal envelope function, i.e., $E_0(\tau)$ has a maximum value of unity. Because the beam is well collimated, the spatial envelope is assumed to depend only on the transverse coordinates $\boldsymbol{\rho} = (x,y)$ and will be written as $E_L(\boldsymbol{\rho})$. This allows simplification of the time-dependent functions in Eqs.. (4a) and (4b) with the use of the following substitutions:

$$\hat{E}_S(\mathbf{r},\tau) = \hat{E}_S'(\mathbf{r},\tau) E_0^*(\tau) , \quad (7a)$$

$$T(\tau) = \int_0^\tau dt |E_0(t)|^2 . \quad (7b)$$

The equations of motion then become

$$\left[\nabla_T^2 + 2ik_S \frac{\partial}{\partial z} \right] \hat{E}_S'(\mathbf{r},T) = -2k_S \kappa_2^* E_L^*(\boldsymbol{\rho}) \hat{Q}(\mathbf{r},T) , \quad (8a)$$

$$\frac{\partial}{\partial T} \hat{Q}(\mathbf{r},T) = -i\kappa_1^* E_L(\boldsymbol{\rho}) \hat{E}_S'(\mathbf{r},T) . \quad (8b)$$

Equation (8b) can be formally integrated and substituted into Eq. (8a), giving

$$\left[\nabla_T^2+2ik_S\frac{\partial}{\partial z}\right]\hat{E}\,'_S(\mathbf{r},T)-ik_S\Gamma g(\rho)\int_0^T dT'\hat{E}\,'_S(\mathbf{r},T')$$

$$=-2k_S\kappa_2^*E_L^*(\rho)\hat{Q}(\mathbf{r},0)\ ,\qquad(9)$$

where $g(\rho)=2\kappa_1^*\kappa_2^*|E_L(\rho)|^2/\Gamma$ is the steady-state gain constant and Γ is the collisional dephasing rate of the Raman transition. Note that the product $\Gamma g(\rho)$ is independent of Γ.

In the transient regime, the Stokes light is temporally transform limited [6,27]. Therefore, to study the spatial distribution of the Stokes field, one can concentrate on the Stokes field near its peak intensity. Since the Stokes field builds up rapidly and smoothly in time with nearly the same shape for each pulse [6], the integral of the Stokes field in Eq. (9) can be approximated by

$$\int_0^{T_m}\hat{E}_S(\rho,T')dT'\approx\hat{E}_S(\rho,T_m)\delta T\ ,\qquad(10)$$

where δT is an effective buildup time for the transient Stokes field, where $T_m\equiv T(\tau_m)$ is evaluated at the time τ_m at the peak of the Stokes pulse as indicated in Fig. 2. Since a transient Stokes field consists of a single temporal mode, the average Stokes intensity profile is proportional to the square of the temporal mode function [27,28]. Thus an expression for δT can be obtained from the average Stokes intensity profile $I_S(\tau)$ by

$$\delta T=\frac{\int_0^{T_m}[I_S(\tau')]^{1/2}|E_0(\tau')|^2d\tau'}{[I_S(\tau_m)]^{1/2}}\ .\qquad(11)$$

The average Stokes intensity profile in the transient regime can be obtained from both classical as well as quantum treatments of SRS [27–29], which give in the high-gain regime the proportionality

$$I_S(\tau)\propto|E_0(\tau)|^2$$
$$\times\exp\left[2\left[2g_0L\Gamma\int_0^\tau dt|E_0(t)|^2\right]^{1/2}\right]\qquad(12)$$

where Γ is the linewidth of the Raman transition. Using parameters of the experiment to calculate $I_S(\tau)$, and numerically integrating Eq. (11) we obtain $\delta T=91$ ps. From Eq. (7b), this value of δT corresponds to a time duration $\delta\tau$ such that $\int_{\tau_m-\delta\tau}^{\tau_m}dt|E_0(t)|^2=\delta T$. Assuming a Gaussian-shaped pump pulse, this gives $\delta\tau=93$ ps, which is indicated in Fig. 2. For a cross check, we observe that this value is close to the half-width of the Stokes intensity profile shown in Fig. 2. The half-width $\tau_{1/2}$ of the Stokes pulse is defined such that $\tau_m-\tau_{1/2}$ is the instant the Stokes intensity is half the peak value. In the high-gain and highly transient limit,

$$T(\tau_m)-T(\tau_m-\tau_{1/2})\approx[(\ln2)^2T(\tau_m)/(2g_0L\Gamma)]^{1/2}\ ,$$

which can be solved for $\tau_{1/2}$. For the case that $E_0(\tau)$ is a step pulse, this reduces to $\tau_{1/2}\approx[(\ln2)^2\tau_m/(2g_0L\Gamma)]^{1/2}$ where τ_m here is the duration of the pump pulse. This is in agreement with results of previous treatments of transient SRS [27].

Equation (9) now becomes

$$\left[\nabla_T^2+2ik_S\frac{\partial}{\partial z}-ik_Sg'(\rho)\right]\hat{E}\,'_S(\mathbf{r})=4\pi\hat{P}(\mathbf{r})\ ,\qquad(13)$$

where $g'(\rho)=2\kappa_1^*\kappa_2^*\delta T|E_L(\rho)|^2$ is the effective transient gain profile, $4\pi\hat{P}(\mathbf{r})=-2k_S\kappa_2^*E_L^*(\rho)\mathbf{Q}(\mathbf{r},0)$ is an effective noise term, and $\hat{E}\,'_S(\mathbf{r})=\hat{E}\,'_S(\mathbf{r},T_m)$.

Equation (13) represents a steady-state-like equation that describes the spatial propagation of a transient Stokes field. The gain medium is described by the same transverse profile as in the steady-state case, but with the important correction that the peak steady-state gain constant $g_0=2\kappa_1^*\kappa_2^*|E_L(0)|^2/\Gamma$ is replaced by an effective value $g_0'=2\kappa_1^*\kappa_2^*\delta T|E_L(0)|^2$. The ratio $g_0'/g_0=\Gamma\delta T<1$ is consistent with the results of previous theories of transient SRS [27]. Thus by concentrating at the instant near the peak of the Stokes pulse, one can use a steady-state-like wave equation with an effective gain coefficient to describe the 3D propagation of a transient Stokes field in a gain-guided medium. This approximation is valid when the condition $\Gamma\tau_L\ll g_0L$ is satisfied to ensure that the Stokes light is transform limited in time.

B. Biorthogonal-mode solution

We have succeeded in putting the transient theory into a form, Eq. (13), that is identical to the steady-state form that has been used previously to describe gain-guided amplifiers [15]. In particular London, Strauss, and Rosen have applied the method of biorthogonal modes [15,20] to the steady-state problem of spatial coherence [17]. Their solution for the Stokes field can now be adapted for the transient case and applied to the problem of beam-pointing fluctuations.

The Stokes field is expanded in terms of a set of eigenmode functions that satisfy the homogeneous, transverse part of Eq. (13),

$$\hat{E}\,'_S(\mathbf{r})=\sum_n\hat{b}_n(z)\psi_n(\rho)\ ,\qquad(14a)$$

$$[\nabla_T^2-ik_Sg'(\rho)]\psi_n(\rho))=-2ik_Sq_n\psi_n(\rho)\ .\qquad(14b)$$

The subscript n in the mode expansion is a shorthand notation for a set of two indices $n=(j,j')$, and the eigenvalue is abbreviated as $q_n\equiv q_{jj'}$. The complex eigenfunctions $\psi_n(\rho)$ are called biorthogonal functions and are different from orthogonal functions. They have the following properties:

$$\int d^2\rho\,\psi_l(\rho)\psi_n(\rho)=\delta_{ln}\ ,\qquad(15)$$

$$B_{ln}\equiv\int d^2\rho\,\psi_l^*(\rho)\psi_n(\rho)\neq\delta_{ln},\quad B_{nn}>1\qquad(16)$$

$$\int d^2\rho\,g'(\rho)\psi_l^*(\rho)\psi_n(\rho)=(q_l^*+q_n)B_{mn}\ .\qquad(17)$$

The operator-valued mode amplitudes $\hat{b}_n(z)$ satisfy

$$\frac{\partial}{\partial z}\hat{b}_n(z)-q_n\hat{b}_n(z)=i\kappa_2^*\hat{Q}_n(z,0)\ ,\qquad(18)$$

where

$$\hat{Q}_n(z,0) = \int d^2\rho\, \hat{Q}(\mathbf{r},0) E_L^*(\rho)\psi_n(\rho) .$$

The solution for the mode amplitude is

$$\hat{b}_n(z,T_m) = \hat{b}_n(z=0,T_m)\exp(q_n z)$$

$$+ i\kappa_2^* \int_0^z dz'\, \exp[q_n(z-z')]\hat{Q}_n(z',0) . \quad (19)$$

The mutual intensity of the Stokes field is, from Eqs. (7a) and (14a),

$$\langle \hat{E}_S^\dagger(\mathbf{r}_1,\tau_m)\hat{E}_S(\mathbf{r}_2,\tau_m)\rangle = |E_0(\tau_m)|^2 \sum_l \sum_n \langle \hat{b}_l^\dagger(z_1,T(\tau_m))\hat{b}_n(z_2,T(\tau_m))\rangle \psi_l^*(\rho_1)\psi_n(\rho_2) , \quad (20)$$

where the shorthand notation is also used to denote $l=(k,k')$, and the eigenvalue $q_l \equiv q_{kk'}$. This convention of $n=(j,j')$ and $l=(k,k')$ will be used throughout the rest of this paper. The correlation functions for the $\hat{b}_n(z,T_m)$ are given by

$$C_{ln} \equiv (2N\kappa_1\delta T/\kappa_2^*)\langle \hat{b}_l^\dagger(z,\tau_m)\hat{b}_n(z,\tau_m)\rangle$$

$$= G_{ln}\{\exp[(q_l^*+q_n)z]-1\}/(q_l^*+q_n) \quad (21)$$

where

$$G_{ln} = \int d^2\rho\, g'(\rho)\psi_l^*(\rho)\psi_n(\rho) . \quad (22)$$

The Stokes power emitted in mode n is proportional to $G_{nn}\int d^2\rho|\psi_n(\rho)|^2 = G_{nn}B_{nn}$. From Eq. (14b), it is easily shown that

$$G_{ln} = (q_l^*+q_n)B_{ln} , \quad (23)$$

so the power emitted per mode is proportional to B_{nn}^2, which is always greater than unity for biorthogonal modes, but is equal to unity for orthonormal modes. This leads to the interpretation that there are B_{nn}^2 photons emitted into mode n in the noise initiation, compared to just one noise photon emitted per mode from normal spontaneous emission that is described by modes which are associated with orthogonal functions. Thus B_{nn}^2 is referred to as the excess-spontaneous-noise factor [14,15]. This interpretation has been recently questioned by Deutch, Garrison, and Wright [20]. They pointed out that while the output power per mode is enhanced by the factor B_{nn}^2, the rate of spontaneous emission for any biorthogonal mode is the same as that for the case of orthogonal modes.

The nondiagonal matrix element B_{ln}, which is the integral between $\psi_l^*(\rho)$ and $\psi_n(\rho)$, is not a Kroneker δ. The correlation function between mode amplitudes b_l and b_n is likewise not Kroneker-δ related. Thus quantum noise excites all the modes in a correlated fashion, rather than in an independent fashion. This is consistent with the fact that the photon-number operators for two distinct biorthogonal modes do not commute with each other [20]. The nondegenerate eigenvalues q_n mean that different transverse modes grow exponentially at different rates. The eigenvalues are directly related to the overlap between the mode functions and the transverse gain profile. This leads to narrowing of the spatial profile, due to the discrimination against the higher-order transverse modes that are amplified less than the lower-order modes which overlap more strongly with the gain profile.

C. Quadratic-gain approximation

The eigensolutions for Eq. (14b) with an arbitrary gain profile can be obtained numerically. For a quadratic-gain profile, which approximates that for a Gaussian profile for regions near the center axis, the eigenfunctions are well known [17,20]. The quadratic approximation treats the outer portion of the medium as purely lossy. This is a reasonable approximation because the higher-order modes occupying the outside portion of the medium have practically very little gain.

Under the quadratic approximation, the transverse gain profile $g'(\rho)$ becomes

$$g'(\rho) \approx g_0'(1-\rho^2/a^2) \quad (24)$$

where a corresponds to the radius of the Gaussian laser intensity transverse profile measured at $1/e$ of its maximum. Assuming azimuthal symmetry, the mode functions factorize $\psi_n(\rho) = \varphi_j(x)\varphi_{j'}(y)$ and the field is given by

$$\hat{E}_S(\mathbf{r},\tau_m) = E_0^*(\tau_m)\sum_{j,j'} \hat{b}_{jj'}(z,\tau_m)\varphi_j(x)\varphi_{j'}(y) . \quad (25)$$

The eigenvalue equation for the mode function in the x coordinate is

$$\left[\frac{d^2}{dx^2} - ik_S g_0'\left[\frac{1}{2} - \frac{x^2}{a^2} \right] \right]\varphi_j(x) = -2ik_S\lambda_j\varphi_j(x) , \quad (26)$$

and similarly for the y coordinate. The solution to Eq. (26) is

$$\varphi_j(x) = \left[\frac{(-iF_e)^{1/4}}{\sqrt{\pi}2^j j!a} \right]^{1/2} \exp\left[-\frac{x^2}{2w^2} \right] H_j(x/w) , \quad (27)$$

where $H_j(x/w)$ is the Hermite polynomial of order j, $F_e = k_S a^2 g_0'$ is an effective Fresnel number defined in terms of the gain length instead of the interaction length, and $w = a/(-iF_e)^{1/4}$ is the complex beam radius. The eigenvalue is given by

$$q_n \equiv q_{jj'} \equiv \lambda_j + \lambda_{j'} = \frac{g_0'}{2}\left[1 - \frac{2j+2j'+1}{(-iF_e)^{1/2}} \right] , \quad (28)$$

where j and j' are non-negative integers.

The effective Fresnel number F_e can be written as $(2\pi a^2/\lambda_S L)(g_0'L)$. The term $2\pi a^2/\lambda_S$ is the Rayleigh range of the Gaussian beam. For a well collimated laser

beam, the interaction length L is shorter than the Rayleigh range. The term $g_0'L$ is the plane-wave gain coefficient of the stimulated process. For a macroscopic Stokes pulse that contains 10^9 photons, $g_0'L$ is around 20. Therefore the effective Fresnel number F_e is always much greater than unity. The real part of the normalized eigenvalue $2q_n/g_0'$ for mode n decreases monotonically with F_e for higher-order modes, and the decrement is proportional to $1/(2F_e)^{1/2}$. Only a finite number of the spatial modes experience gain, i.e., those satisfying $\mathrm{Re}(q_n) > 0$.

The matrix element $B_{ln} \equiv \beta_{kj}\beta_{k'j'}$ can be evaluated analytically with the help of the recurrence relation of the Hermite polynomials. The matrix element

$$\beta_{kj} = \int_{-\infty}^{\infty} dx\ \varphi_k^*(x)\varphi_j(x) \tag{29a}$$

satisfies the recurrence relation

$$\beta_{kj} = \sqrt{(k-1)/k}\ \frac{\alpha-\alpha^*}{\alpha+\alpha^*}\beta_{k-2,j}$$

$$+\sqrt{n/k}\ \frac{2|\alpha|}{\alpha+\alpha^*}\beta_{k-1,j-1}\ , \tag{29b}$$

where $\alpha = w^{-2}$ and $k \geq j$. A similar recurrence relation applies for the case $k < j$.

The matrix element G_{ln} defined in Eq. (22) must be evaluated properly to ensure that the equivalent noise input has positive intensity for all modes. This can be achieved by using the actual Gaussian gain profile instead

of the quadratic profile in Eq. (22). The matrix element $G_{ln} \equiv \gamma_{kj}\gamma_{k'j'}$ is given by matrix element

$$\gamma_{kj} = \int_{-\infty}^{\infty} dx\ g'(x)\varphi_k^*(x)\varphi_j(x)\ , \tag{30a}$$

which can be evaluated by

$$\gamma_{kj} = \sqrt{(k-1)/k}\ \frac{\alpha-\alpha^*-2}{\alpha+\alpha^*+2}\gamma_{k-2,j}$$

$$+\sqrt{n/k}\ \frac{2|\alpha|}{\alpha+\alpha^*+2}\gamma_{k-1,j-1}\ . \tag{30b}$$

The first four biorthogonal-mode functions in the quadratic-gain approximation are shown in Figs. 6 and 7. The higher-order mode functions increasingly shift away from the center axis. The normalized modal gains $2\,\mathrm{Re}(q_{j0}/g_0')$ for these modes are listed in Tables I and II. [The eigenvalue $q_n \equiv q_{j0}$ is associated with the function $\psi_n(\rho) = \varphi_j(x)\varphi_0(y)$.] It is close to unity for the lowest-order mode and decreases linearly for higher-order mode functions as the overlap between these functions and the gain profile becomes less. The area under the curve $|\varphi_j(x)|^2$ increases for higher-order mode functions; this reflects the fact that the excess-noise factor increases for higher-order modes. The narrowing of the mode functions due to increasing gain can be seen in Fig. 7.

The transverse profile of the average Stokes intensity, calculated from Eq. (20) with $y = 0$, is shown in Fig. 8. The narrowing of the Stokes profile for higher gain is due
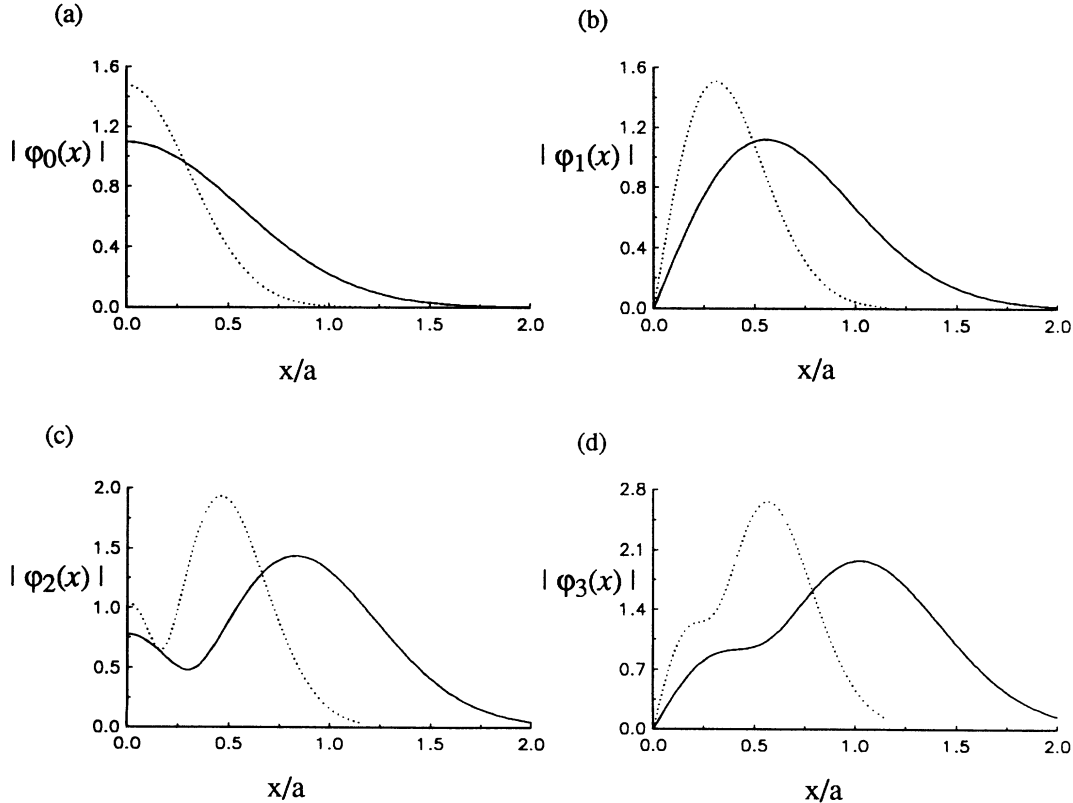

FIG. 6. The first four transverse biorthogonal-mode functions are plotted as a function of the normalized transverse coordinate x/a for two different Fresnel numbers. The solid curves are for Fresnel number $F = 0.33$, the dotted curves are for $F = 3.5$. The transient gain $g_0'L$ is 22.

TABLE I. The normalized modal gain $2\,\mathrm{Re}(q_{j0}/g_0')$ for the first four mode functions with $g_0'L = 22$ and two different Fresnel numbers.

	$2\,\mathrm{Re}(q_{00}/g_0')$	$2\,\mathrm{Re}(q_{10}/g_0')$	$2\,\mathrm{Re}(q_{20}/g_0')$	$2\,\mathrm{Re}(q_{30}/g_0')$
$F = 0.33$	0.845	0.535	0.224	-0.086
$F = 3.5$	0.953	0.858	0.763	0.668

to greater differential in the normalized model gain at higher Stokes gain $g_0'L$, which is shown in Table II.

D. Beam-slice description

Since we are interested in the beam-pointing fluctuations in the x-z plane (at $y = 0$), it is convenient to define reduced mode amplitudes

$$\hat{b}_j'(z,\tau_m) = \sum_{j'} \hat{b}_{jj'}(z,\tau_m)\varphi_{j'}(y=0) . \tag{31}$$

In terms of these reduced mode amplitudes, the Stokes field is expressed in the $y = 0$ slice as

$$\hat{E}_S(x,z,\tau_m) = E_0^*(\tau_m) \sum_j \hat{b}_j'(z,\tau_m)\varphi_j(x) . \tag{32}$$

The mutual intensity becomes, in the $y = 0$ slice,

$$\langle \hat{E}_S^\dagger(x_1,z,\tau_m)\hat{E}_S(x_2,z,\tau_m) \rangle$$

$$= \frac{\kappa_2^*}{2N\kappa_1\delta T}|E_0(\tau_m)|^2 \sum_{k,j} C_{kj}'\varphi_k^*(x_1)\varphi_j(x_2) \tag{33}$$

where

$$C_{kj}' = \sum_{k',j'} \varphi_{k'}^*(y=0)C_{kk'jj'}\varphi_{j'}(y=0) \tag{34}$$

where $C_{kk'jj'} \equiv C_{ln}$. It should be noted that the one-dimensional description expressed by Eqs. (32) and (34) is distinct from a treatment of a wave equation that neglects the y coordinate altogether.

IV. THEORY OF BEAM-POINTING FLUCTUATIONS OF SRS

The solution for the Stokes field given by Eq. (32) can be used to calculate the statistics of the beam-pointing angles. The direction of the flow of energy associated with an optical field is described by the Poynting vector

$$\mathbf{S}(\mathbf{r},\tau) = \frac{c}{8\pi}\mathbf{E}^*(\mathbf{r},\tau)\times\mathbf{H}(\mathbf{r},\tau) , \tag{35}$$

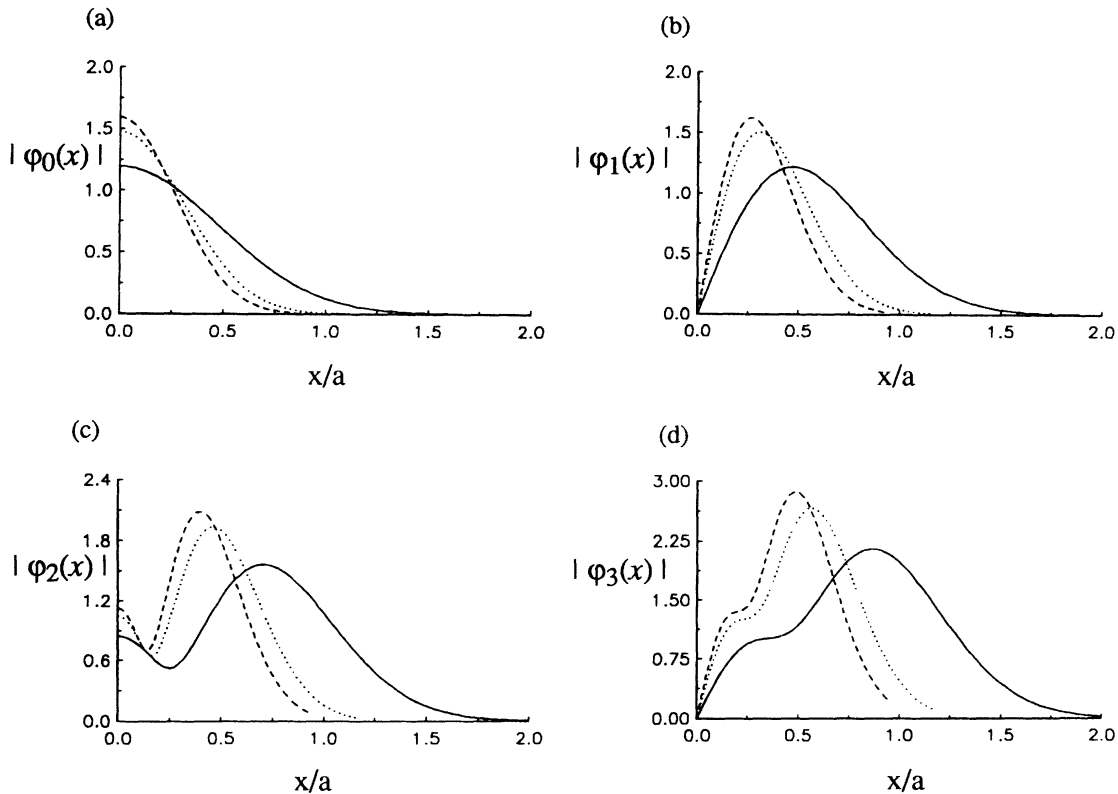where $\mathbf{H}(\mathbf{r},\tau)$ is the magnetic field. For a linearly polar-

FIG. 7. The first four transverse biorthogonal-mode functions are plotted as a function of the normalized transverse coordinate x/a for three effective gain values. The solid curves are for $g_0'L = 4$, the dotted curves are for $g_0'L = 22$, the dashed curves are for $g_0'L = 40$. The Fresnel number F is 3.5

TABLE II. The normalized modal gain $2\operatorname{Re}(q_{j0}/g_0')$ for the first four mode functions with $F = 3.5$ and three different effective gain values.

	$2\operatorname{Re}(q_{00}/g_0')$	$2\operatorname{Re}(q_{10}/g_0')$	$2\operatorname{Re}(q_{20}/g_0')$	$2\operatorname{Re}(q_{30}/g_0')$
$g_0'L = 4$	0.889	0.667	0.445	0.223
$g_0L = 22$	0.953	0.858	0.763	0.668
$g_0'L = 40$	0.965	0.895	0.824	0.754

ized field propagating along the z axis, the electric field vector can be written as

$$\mathbf{E}_S(\mathbf{r},\tau) = \hat{\mathbf{e}} E_S(\mathbf{r},\tau)\exp(ik_S z - i\omega_S \tau) , \tag{36}$$

where $\hat{\mathbf{e}}$ is the unit vector of the polarization of the electric field. The component of the Poynting vector transverse to the direction of propagation is equal to

$$\mathbf{S}_T(\mathbf{r},\tau) = -i\frac{c^2}{8\pi\mu_0\omega_S}E_S^*(\mathbf{r},\tau)\nabla_T E_S(\mathbf{r},\tau) . \tag{37}$$

It describes both the direction of the energy flow and the magnitude of the energy flux.

For Raman generation, the fluctuation of the Poynting vector is due to both the pulse-energy fluctuation and the beam-pointing-angle fluctuation. The beam-pointing angle associated with the Stokes field at the output face of the Raman generator was defined by Walmsley to be $[(\mathbf{K}_T)_x^2 + (\mathbf{K}_T)_y^2]^{1/2}/k_S$, where $(\mathbf{K}_T)_x$ is given by Eq. (1a) in the Introduction. It is proportional to the mean, normalized, transverse Poynting vector. The normalization by the pulse energy allows one to characterize the beam-pointing angle for a single realization and determine its statistics over an ensemble of realizations.

Walmsley's definition of the mean transverse k vector given by Eq. (1a) relates to the Stokes beam as a whole (both x and y directions). Its statistics can be calculated theoretically using the solution given by Eq. (25), and can be measured experimentally by recording the spatial distribution (both x and y directions) of the Stokes intensity for a number of realizations. In contrast, our interferometric technique measures the beam-pointing fluctuations in the x-z plane, for a fixed value of y. The definition of the beam-pointing angle corresponding to this measurement is K_x/k_S, where K_x is given by Eq. (2),
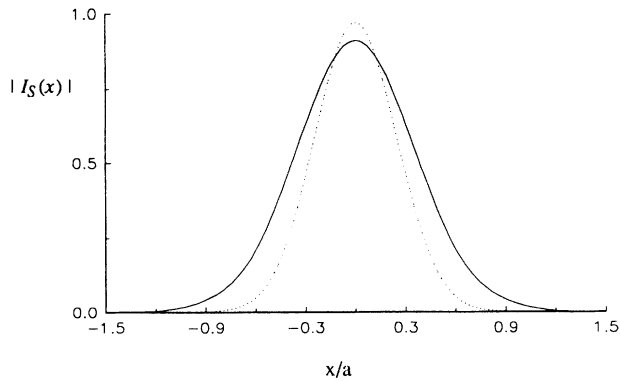
and a slice of the Stokes field distribution at $y = 0$ is used.

K_x can be expressed in terms of the complex mode amplitudes $\hat{b}_j'$, appearing in Eq. (31). For purposes of statistical averaging of normally ordered correlation functions, it is known that the operators $\hat{b}_j'$ can be replaced by a corresponding set of complex random variables $\{b_j'\}$ having Gaussian statistics [28,30]. This essentially follows from the thermal-like nature of unsaturated SRS. For the set of mutually Gaussian variables, the joint probability distribution $P(\{b_j'\})$ is given by

$$P(\{b_j'\}) = \left[\prod_j \frac{1}{\pi}\right]\frac{1}{\det(\underline{C}')}\exp\left[-\sum_k \sum_j b_k'^* C_{kj}'^{-1} b_j'\right] , \tag{38}$$

where $\underline{C}'^{-1}$ is the inverse of the correlation matrix $\underline{C}'$, whose elements $C_{kj}' = \langle b_k'^* b_j'\rangle$ are evaluated by Eqs. (21) and (30b). The transverse k value K_x then becomes

$$K_x = \frac{\sum_k \sum_j b_k'^* b_j' D_{kj}}{\sum_k \sum_j b_k'^* b_j' B_{kj}} , \tag{39}$$

where $B_{kj} = \beta_{kj}$ is given in Eq. (29a), and

$$D_{kj} = -i\int dx \, \varphi_k^*(x)\frac{d}{dx}\varphi_j(x) , \tag{40}$$

which can be evaluated analytically for the quadratic-gain eigenfunctions.

The probability density for finding K_x having a value K_x' is

$$P(K_x') = \langle \delta(K_x - K_x')\rangle = \frac{1}{2\pi}\int d\xi \exp(-i\xi K_x')\langle e^{i\xi K_x}\rangle , \tag{41}$$

where the characteristic function is, using matrix notation,

$$\langle e^{i\xi K_x}\rangle = \int \frac{d^2 b}{\pi}\exp\left[i\xi\frac{\underline{b}^\dagger \underline{D} \, \underline{b}}{\underline{b}^\dagger \underline{B} \, \underline{b}}\right]P(\underline{b}) , \tag{42}$$

and $\int d^2 b/\pi$ is the shorthand form of $\prod_j (\int d^2 b_j'/\pi)$. The probability distribution function, after some algebraic manipulation, is found to be (see Appendix)

$$P(K_x') = \frac{1}{\det(\underline{C})\det(\underline{B})}$$
$$\times \int \frac{d\xi}{2\pi}\frac{\partial}{\partial(i\xi K_x')}$$
$$\times \frac{1}{\det(\underline{C}^{-1}\underline{B}^{-1} + i\xi\underline{D}\,\underline{B}^{-1} - i\xi K_x'\underline{I})} , \tag{43}$$

FIG. 8. The transverse profile of the average Stokes intensity at $y = 0$ for two different transient gains at Fresnel number 3.5: solid curve is for transient gain $g_0'L = 22$, and dotted curve is for $g_0'L = 38$.

where $\underline{I}$ is the identity matrix. The matrices $\underline{B}$, $\underline{C}$, and $\underline{D}$ are all Hermitian, the matrix elements $B_{kj} = \beta_{kj}$, and C_{kj}, D_{kj} are given by Eqs. (29b), (34), and (40).

The integral in Eq. (43) can be numerically evaluated to determine the probability density $P(K'_x)$. For an interaction region of moderate Fresnel number, only a finite number of the eigenvalues have q_n a positive real part. This makes numerical evaluation of $P(K'_x)$ using Eq. (43) relatively manageable by neglecting all the nonamplifying modes.

The probability density function $P(K'_x)$ for transverse k value is plotted in Fig. 9 for three different Fresnel numbers. For a small Fresnel number, $F = 0.74$, the lowest-order mode dominates over all the higher-order modes. This is due to the relatively large decrement of the normalized modal gain, 0.21 (see Table I), and the high effective gain value $g'_0 L$ of 22. The mode occupation for the lowest-order mode is found to be greater than 0.95, and this is reflected in the sharply peaked probability density function shown in the solid curve. As the Fresnel number of the interaction region increases, the modal gain decrement becomes smaller. The presence of the higher-order modes becomes more important. This leads to the broadening of the probability distribution and larger beam-pointing fluctuations. Thus the beam-pointing fluctuation is caused by the presence of many spatial modes that are excited with random, but correlated, amplitudes and phases.

Figure 10 shows as a solid curve the standard deviation ΔK_x of the transverse k value calculated using the probability density $P(K'_x)$ in Eq. (43). As expected, the increase of ΔK_x with Fresnel number results from the increasing number of modes contributing to the distortion of the field wave front.

V. COMPARISON OF THEORY AND EXPERIMENT

Because the quantity $\bar{k}_x$ [Eq. (3)] measured by the two-beam interference technique is not identical to that defined as $K_{x1} - K_{x2}$ in Sec. IV using Eq. (2), we sought to check how closely these two quantities agree theoretically before comparing to the experiment. Furthermore, because the numerical computations leading to ΔK_x are rather complicated, we sought an alternative way to cal-
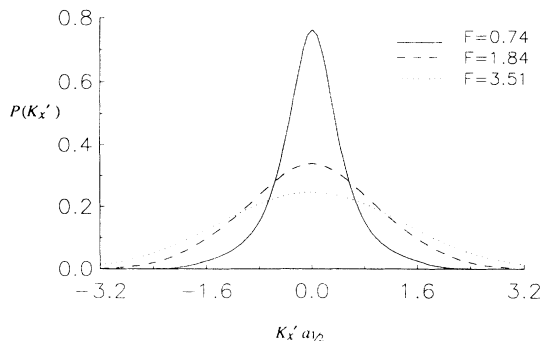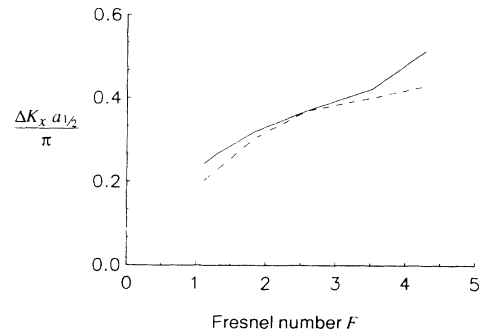

FIG. 10. Standard deviation of the mean transverse k value K'_x vs Fresnel number. The solid curve is calculated from Eq. (43). The dashed curve is calculated from numerical simulations of the two-beam interference experiment using Eqs. (32) and (38) to generate the field and the same procedure involving Eq. (3) as that used to analyze the two-beam experimental data. The ordinate can be interpreted as the standard deviation of the beam-pointing angle divided by its diffraction-limited angle.

culate ΔK_x as a check on the accuracy of our method. Both of these checks were accomplished by carrying out numerical simulations of the experimental quantity $\bar{k}_x$. We generated random realizations of two independent Stokes fields by using Eqs. (32) and a random-number generator to simulate the $\{b'_j\}$ coefficients, using Eq. (38) as the probability density. We then calculated the resulting interference pattern and treated it in identical fashion to an actual experimental pattern, i.e., calculated $\bar{k}_x$ from Eq. (3). In similar fashion to the experiment, we repeated this procedure several hundred times to obtain the standard deviation $\Delta K_x = \Delta \bar{k}_x / \sqrt{2}$, and the results are plotted in Fig. 10 as the dashed curve. The agreement with the theoretical result in the solid curve is satisfactory, indicating that the theory is likely free of numerical error, and that the theoretical and experimental quantities of study are essentially the same.

The solid curve in Fig. 5 is the standard deviation ΔK_x of the transverse k value calculated using the theoretical probability density function $P(K'_x)$ in Eq. (43). All parameters in the calculation are taken to be equal to those measured. While the trend of the data and theory agrees, there is absolute agreement only at the large Fresnel numbers. The systematic disagreement at low Fresnel number is likely caused by the limited dynamic range of the data-collection instrumentation, which was limited by noise at the low-intensity end and by camera saturation at the high end. This biases the ensemble for which data can be collected. Simulation studies support this conclusion [31]. Another potential source of disagreement is the use in the theory of a parabolic gain profile rather than the actual profile.

VI. COMPARISON OF ALTERNATIVE DEFINITIONS AND METHODS FOR CALCULATING BEAM-POINTING FLUCTUATIONS

It is worth comparing the behavior of the beam-pointing angle for a slice of the Stokes beam, as measured

FIG. 9 Probability density function of the mean transverse k value K'_x for the $y = 0$ beam slice, from Eq. (43), plotted for three different Fresnel numbers. The transient gain $g'_0 L$ is 22.

here, to that for the whole beam as treated theoretically by Walmsley [10]. The method for calculating the beam-pointing angle for the whole beam [defined by Eq. (1a)] is similar to that presented above for the case of a slice of the Stokes beam. In this case, the matrix elements B_{ln}, C_{ln}, and D_{ln} are given by $B_{ln} \equiv \beta_{kj}\beta_{k'j'}$, Eq. (30a), and $D_{ln} = D_{kj}\beta_{k'j'}$. The prediction of the standard deviation of the beam-pointing angle versus Fresnel number for the case of single-slice and whole-beam Stokes output is shown in Fig. 11. The fluctuation of the beam-pointing angle for a beam slice at $y = 0$ tends to increase more than that of the whole beam as the Fresnel number increases. The beam-pointing angle for the whole beam can be loosely viewed as an average of the single-slice beam angle over different y coordinates. The beam-pointing angle for a realization can be positive or negative, and for large Fresnel number the fluctuations of the beam angle of different slices are roughly independent. As the Fresnel number increases, the number of different slices also increases, and the fluctuations of the beam-pointing angle averaged over many independent slices will be smaller than that of a single slice.

The beam-pointing fluctuations predicted by the biorthogonal-mode solutions of the Stokes field should also be contrasted to that predicted by the orthogonal-mode solutions of the theory by Raymer *et al.* (RWMS) which treats the SRS problem for a uniform gain profile [27]. The standard deviation of the x component of the normalized k vector for a whole beam using the solutions of the RWMS theory was calculated by Walmsley [10,32]. Figure 12 compares the whole-beam-pointing fluctuations versus the Fresnel number as predicted by the two theories. The biorthogonal-mode theory is expected to be a more accurate description. Three aspects of these theories distinguish them: (1) the scaling of the number of the positive-gain modes with Fresnel number (see Sec. VII), (2) the correlations of the modes, and (3) the strength of the noise in each mode. It is interesting to note that with these different factors present the two theories give results within 20% of each other.

FIG. 12. Standard deviation of the x component of the mean transverse k vector $(\mathbf{K}_T)_x$ vs the Fresnel number as predicted by the biorthogonal-mode theory of this paper and the orthogonal-mode theory of RWMS. The solid curve is calculated using the solution of the field from the biorthogonal theory; the dashed curve is calculated using the solution of the field from the RWMS theory with orthogonal modes [10,32]. The transient gain $g_0'L$ is 22.

VII. CONCLUSIONS AND DISCUSSION

The beam-pointing fluctuations of a Raman-amplifier output have been measured using an interferometric method. The agreement with the theoretical treatment demonstrates that the beam-pointing jitter is caused by quantum noise. The observed beam-pointing fluctuation of light from transient SRS increases with increasing Fresnel number, and at $F = 5$ the fluctuation is about 50% of the diffraction-limited angle defined by the pump-beam aperture. The increase in beam-pointing fluctuations with increasing Fresnel number could have significant implications in cavityless x-ray lasers, which have dynamics similar to SRS, but usually have much larger Fresnel number because of the shorter wavelength. Such high-Fresnel-number experiments can further test the validity of the theories.

A treatment of the three-dimensional, spatial propagation of transient SRS has been developed. The transverse eigenmodes of a gain-guided Raman amplifier are biorthogonal, and the mode amplitudes are consequently correlated. This contrasts with the orthogonal modes of the RWMS theory, which propagate in a free-space-like medium, and are consequently independent. The Gaussian-shaped gain distribution leads to a discrimination of modes, with those concentrated on the axis having higher gain. This reduces the number of excited modes, and thus reduces the beam-pointing fluctuations relative to the case of a uniformly pumped volume.

The trend of growing beam-pointing-angle fluctuations with increasing Fresnel number is due to the presence of more spatial modes being excited simultaneously in the interaction region. When the Fresnel number is small, the lowest-order mode has an amplitude that is much greater than the higher-order modes, due to its higher gain. The beam-pointing-angle fluctuation is then determined predominantly by the ratio of the amplitudes be-
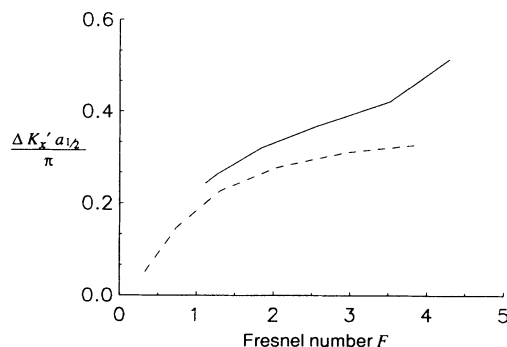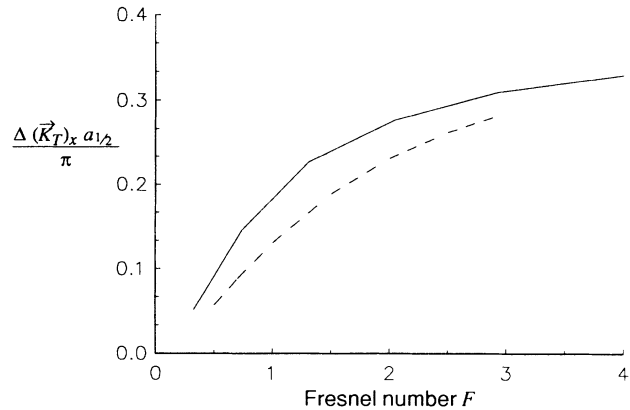
FIG. 11. Standard deviation of the normalized beam-pointing angle vs Fresnel number. The solid curve is calculated using the single-slice definition, Eq. (2), of the mean transverse k value; the dashed curve is calculated using the whole-beam definition, Eq. (1a), of the mean transverse k vector $(\mathbf{K}_T)_x$. Both curves are obtained using the biorthogonal, gain-guided modes. The transient gain $g_0'L$ is 22.

tween the second strongest mode and the lowest-order mode; this ratio is equal to $\exp[-g_0'L/(2F_e')^{1/2}]$. As the Fresnel number increases, the normalized modal gain decrement decreases as $(2F_e')^{-1/2}$, and the contributions from higher-order modes give rise to increasing fluctuations in the beam-pointing angle.

It is worth noting that the number of spatial modes having positive gain grows slowly, approximately proportional to F. In contrast, the number of spatially coherent (orthogonal) modes that occupy the output plane of a cylindrical region of cross-sectional area $\pi a_{1/2}^2$ and length L is proportional to F^2, according to the RWMS theory [27], which treats the 3D propagation in a uniformly pumped Raman medium in a manner similar to wave propagation in free space.

It should be pointed out that the beam-pointing-angle fluctuation is about three orders of magnitude larger than that observed for a stable-cavity laser [33]. It is related to the enhancement effect of the spectral power output of

semiconductor lasers in that both originate from quantum-mechanical uncertainty, and the eigenmodes are shaped by the gain coupling of the medium and the field.

ACKNOWLEDGMENTS

APPENDIX

To obtain Eq. (43), Eq. (41) can be written as

$$P(K_x') = \langle \underline{b}^\dagger \underline{B}\, \underline{b}\, \delta(K_x'\underline{b}^\dagger \underline{B}\, \underline{b} - \underline{b}^\dagger \underline{D}\, \underline{b}) \rangle . \tag{A1}$$

Using the properties of the δ function, Eq. (A1) becomes

$$P(K_x') = \left\langle \frac{1}{2\pi} \int d\xi \frac{\partial}{\partial(i\xi K_x')}\exp(-i\xi\underline{b}^\dagger \underline{D}\, \underline{b} + i\xi K_x'\underline{b}^\dagger \underline{B}\, \underline{b}) \right\rangle . \tag{A2}$$

Substituting Eq. (38) into Eq. (A2), the probability density function becomes

$$P(K_x') = \frac{1}{\det(\underline{C'})} \int \frac{d^2\underline{b}}{\pi}\exp(-\underline{b}^\dagger \underline{C}'^{-1}\underline{b})\frac{1}{2\pi}\int d\xi \frac{\partial}{\partial(i\xi K_x')}\exp(-i\xi\underline{b}^\dagger \underline{D}\, \underline{b} + i\xi K_x'\underline{b}^\dagger \underline{B}\, \underline{b}) . \tag{A3}$$

Exchanging the order of integration and rearranging the terms in the argument of the exponential function, Eq. (A3) becomes

$$P(K_x') = \frac{1}{2\pi \det(\underline{C'})}$$
$$\times \int d\xi \frac{\partial}{\partial(i\xi K_x')}$$
$$\times \int \frac{d^2\underline{b}}{\pi}\exp[-\underline{b}^\dagger(\underline{C}'^{-1} + i\xi\underline{D} - i\xi K_x'\underline{B})\underline{b}] .$$
$$\tag{A4}$$

Defining

$$T(\xi) \equiv \underline{C}^{-1} + i\xi\underline{D} - i\xi K_x'\underline{B} ,$$

which is a non-Hermitian matrix, the identity

$$\int \frac{d^2\underline{b}}{\pi}\exp\{-[\underline{b}^\dagger \underline{T}(\xi)\underline{b}]\} = 1/\det[T(\xi)]$$

holds for a certain class of the non-Hermitian matrix $\underline{T}(\xi)$. This condition is satisfied for the matrices treated in this problem. See [31] for more detail. This leads to Eq. (43).

[1] H. M. Gibbs, Q.H.F. Vrehen, and H.M.S. Hickspoor, Phys. Rev. Lett. **39**, 547 (1977).

[2] S. P. Kravis and L. Allen, Opt. Commun. **23**, 289 (1977).

[3] I. A. Walmsley and M. G. Raymer, Phys. Rev. Lett. **50**, 962 (1983).

[4] N. Fabricius, K. Nattermann, and D. von der Linde, Phys. Rev. Lett. **52**, 113 (1984).

[5] A. S. Grabchikov, S. Ya. Kilin, V. P. Kozich, and N. M. Iodo, Pis'ma Zh. Eksp. Teor. Fiz. **43**, 3 (1986) [JETP Lett. **43**, 151 (1986)].

[6] M. G. Raymer, Z. W. Li, and I. A. Walmsley, Phys. Rev. Lett. **63**, 1586 (1989).

[7] D. C. MacPherson, R. C. Swanson, and J. L. Carlsten, Phys. Rev. Lett. **61**, 66 (1988).

[8] M. A. Henesian, C. D. Swift, and J. R. Murray, Opt. Lett. **10**, 565 (1985).

[9] S. J. Kuo, C. Radzewicz, and M. G. Raymer (unpublished).

[10] I. A. Walmsley, J. Opt. Soc. Am. B **8**, 805 (1991); **8**, 2392 (1991).

[11] S. J. Kuo, D. T. Smithey, and M. G. Raymer, Phys. Rev. Lett. **66**, 2605 (1991).

[12] A. E. Siegman, Phys. Rev. A **39**, 1253 (1989).

[13] W. A. Hamel and J. P. Woerdman, Phys. Rev. A **40**, 2785 (1989); Phys. Rev. Lett. **64**, 1506 (1990).

[14] K. Petermann, IEEE J. Quantum Electron. **15**, 566 (1979).

[15] H. Haus and S. Kawakami, IEEE J. Quantum Electron. **21**, 63 (1985).

[16] W. Streifer, D. R. Serfres, and R. D. Burnham, Appl. Phys. Lett. **40**, 305 (1985).

[17] R. A. London, M. Strauss, and M. D. Rosen, Phys. Rev. Lett. **65**, 563 (1990).

[18] M. D. Feit and J. A. Fleck, Jr., J. Opt. Soc. Am. B **7**, 2048 (1990).

[19] C. H. Henry, J. Lightwave Technol. **LT-4**, 288 (1986).

[20] I. V. Deutch, J. C. Garrison, and E. M. Wright, J. Opt. Soc. Am. B **8**, 1244 (1991).

[21] B. N. Perry, P. Rabinowitz, and M. Newstein, Phys. Rev. A **27**, 1989 (1983).

[22] M. Strauss, J. Oreg, and A. Bar-Shalom, Phys. Rev. A **38**, 4712 (1988).

[23] M. G. Raymer and J. Mostowski, Phys. Rev. A **24**, 1980 (1981).

[24] T. Sizer II and I. N. Duling III, IEEE J. Quantum Electron. **24**, 404 (1988).

[25] W. K. Bischel and M. T. Dyer, J. Opt. Soc. Am. B **3**, 677 (1986).

[26] S. J. Kuo, D. T. Smithey, and M. G. Raymer, Phys. Rev. A **43**, 4083 (1991).

[27] M. G. Raymer, I. A. Walmsley, J. Mostowski, and B. Sobolewska, Phys. Rev. A **32**, 332 (1985).

[28] For review, see M. G. Raymer and I. A. Walmsley, in *Progress in Optics*, edited by E. Wolf (North-Holland Elsevier, Amsterdam, 1990), Vol. XXVIII.

[29] C. S. Wang, in *Quantum Electronics: A Treatise*, edited by H. Rabin and C. L. Tang (Academic, New York, 1975), Vol. 1.

[30] F. Haake and R. J. Glauber, Phys. Lett. **68A**, 29 (1979); F. Haake, H. King, G. Schroder, and R. J. Glauber, Phys. Rev. A **20**, 2047 (1979).

[31] S. J. Kuo, Ph.D. thesis, University of Rochester, 1991.

[32] Walmsley's results for the standard deviation of $|\mathbf{K}_T|$ are scaled by $(\sqrt{2}\pi)^{-1}$ in order to compare with our results for $(\mathbf{K}_T)_x$.

[33] M. D. Levenson, W. H. Richardson, and S. H. Perlmutter, Opt. Lett. **14**, 779 (1989).
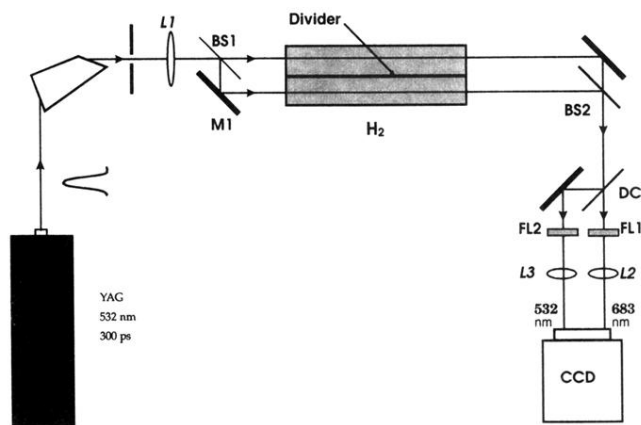
FIG. 1. Apparatus for generating two independent Stokes beams which are combined to produce an interference pattern, whose spatial frequency is indicative of the relative angle between the two beams. Interference patterns of Stokes light and pump light are recorded on a CCD camera.
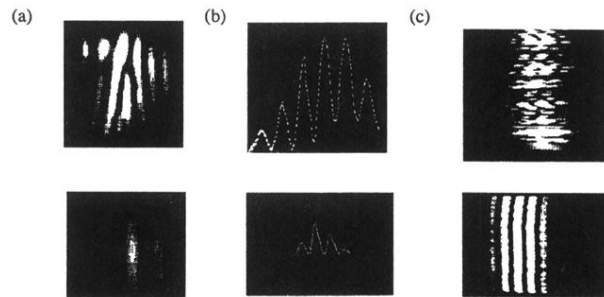
FIG. 3. Single-shot interference patterns of Stokes light and pump light recorded by the CCD camera: Stokes patterns in upper half, pump patterns in lower half (a) interference patterns from a single shot, (b) flux density $J(x)$ obtained from a single-pixel-wide trace of (a), (c) two-pixel-wide samples of interference patterns from 100 successive shots.